






RESEARCH ARTICLE | NOVEMBER 15 2023

Exploring the spin dynamics of a room-temperature diamond maser using an extended rate equation model

Yongqiang Wen ; Philip L. Diggle ; Neil McN. Alford ; Daan M. Arroo  

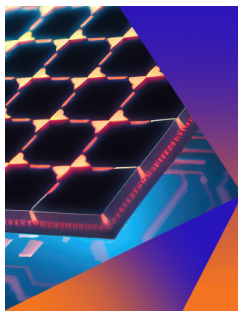


J. Appl. Phys. 134, 194501 (2023)

<https://doi.org/10.1063/5.0164930>



CrossMark



Applied Physics Letters

Special Topic:
Hybrid and Heterogeneous Integration in Photonics:
From Physics to Device Applications

Submit Today

Exploring the spin dynamics of a room-temperature diamond maser using an extended rate equation model

Cite as: J. Appl. Phys. **134**, 194501 (2023); doi: [10.1063/5.0164930](https://doi.org/10.1063/5.0164930)

Submitted: 25 June 2023 · Accepted: 17 October 2023 ·

Published Online: 15 November 2023



Yongqiang Wen,^{1,2} Philip L. Diggle,^{1,2} Neil McN. Alford,^{1,2} and Daan M. Arroo^{1,2,a)}

AFFILIATIONS

¹Department of Materials, Imperial College London, Exhibition Road, London SW7 2AZ, United Kingdom

²London Centre for Nanotechnology, 17-19 Gordon Street, London WC1H 0AH, United Kingdom

^{a)}Author to whom correspondence should be addressed: d.arroo14@imperial.ac.uk

ABSTRACT

Masers—the microwave analog of lasers—are coherent microwave sources that can act as oscillators or quantum-limited amplifiers. Masers have historically required high vacuum and cryogenic temperatures to operate, but recently, masers based on diamond have been demonstrated to operate at room temperature and pressure, opening a route to new applications as ultra-low noise microwave amplifiers. For these new applications to become feasible at a mass scale, it is important to optimize diamond masers by minimizing their size and maximizing the power of signals that can be amplified. Here, we develop and numerically solve an extended rate equation model to present a detailed phenomenology of masing dynamics and determine the optimal properties required for the copper cavity, dielectric resonator, and gain medium in order to develop portable maser devices. We conclude by suggesting how the material parameters of the diamond gain media and dielectric resonators used in diamond masers can be optimized, and how rate equation models could be further developed to incorporate the effects of temperature and nitrogen concentration on spin lifetimes.

© 2023 Author(s). All article content, except where otherwise noted, is licensed under a Creative Commons Attribution (CC BY) license (<http://creativecommons.org/licenses/by/4.0/>). <https://doi.org/10.1063/5.0164930>

I. INTRODUCTION

Due to their long spin relaxation times, negatively charged nitrogen-vacancy defect centers (NV⁻) in diamonds^{1,2} have been widely used as a room-temperature material for quantum metrology,^{3–5} communications,⁶ and quantum information processing.^{7–9} Recently, their use has been extended to the microwave analog of lasers, known as masers, by placing NV-enriched diamonds into dielectric resonators and enclosing the system in a copper cavity.¹⁰ Although masers are unmatched for low-noise microwave amplification, their use has historically been limited to niche applications in deep space communications and radio astronomy due to the need for high vacuum and cryogenic temperatures required to allow them to operate. The demonstration of room-temperature masers based on organic^{11–13} and inorganic^{10,14–17} gain media, thus opens up a path to the widespread use of masers as ultra-low noise microwave amplifiers, which in addition to existing applications in radio astronomy and communications technology, are of increasing interest for the low-power microwave signal processing essential to many quantum technologies.¹⁸ In this latter regard, masers

may offer an advantage over Josephson parametric amplifiers, which have a limited dynamic range and are easily saturated compared to masers.¹⁹

The NV⁻ defect is a $S = 1$ spin center that can be described using a seven-level Hamiltonian consisting of a ground-state triplet, an excited-state triplet, and an intermediate singlet state. NV⁻ defects can be photoexcited to the excited state triplet using laser pulses with wavelengths at or below 637 nm, from which they may relax either through a spin-conserving radiative decay or through a spin-selective non-radiative decay whose net effect is to preferentially transfer electrons from the excited $m_s = \pm 1$ states to the $m_s = 0$ ground state via the intermediate singlet state, as seen in Fig. 1. These spin-selective transitions mean that NV⁻ centers can be optically controlled and read out. The NV⁻ defect exhibits a long T_1 spin-lattice relaxation time (up to 6 ms²⁰) and T_2 spin-spin relaxation time (0.6 ms for diamonds that with a natural abundance of ¹³C and an NV concentration of 3×10^{13} cm⁻³, though this may be extended to 1.8 ms in isotopically purified ¹²C diamond at lower

22 February 2024 14:16:02

NV concentrations^{21,22}) at room temperature. It is these properties that allow an ensemble of NV⁻ defects placed in a dielectric resonator cavity in an applied magnetic field to be used as a gain medium for a room-temperature maser, as well as for lasers.²³ The threshold laser power with which an NV ensemble must be pumped to allow steady-state masing is proportional to $(T_1(C-1))^{-1}$, so that it depends on the spin-lattice relaxation time and a figure of merit known as the cooperativity C , defined as¹⁰

$$C = 4g^2N/(\kappa_c\kappa_s), \quad (1)$$

where g is the spin-photon coupling strength between each active NV⁻ spin and the cavity field, N is the number of NV⁻ spins for which the masing transition between the $m_s = 0$ and $m_s = -1$ ground state sub-levels is resonant with the cavity (for a field aligned with one of the four possible directions of the NV axis, this corresponds to 1 in 12 NV spins, since in general only one of the three ¹⁴N hyperfine transitions will be resonant with the cavity), $\kappa_c = \omega/Q$ is cavity loss rate, ω is the resonant frequency of the cavity, Q is the quality factor of the resonator, and κ_s is the dephasing rate of the spins.¹⁰ The cooperativity measures the ratio of the coupling effect of N spins and the combined decoherence rates and by inspecting the expression for the threshold laser pump power, it can be seen that masing requires the cooperativity to be larger than one. To achieve this, we can either increase the coupling by having a smaller mode volume or more NV⁻ spins or a higher Q factor to reduce the decoherence rate. The copper cavity in which the diamond and resonator are enclosed acts as a shield that reduces radiation losses, increasing the quality factor Q and hence the cooperativity.

Despite impressive experimental demonstrations and characterization of room-temperature diamond masers,^{10,16,17} certain challenges for the widespread adoption of diamond masers have been identified spanning materials challenges such as making diamond gain medium with a sufficient amount of photostable NV⁻ centers under optical excitation as well as engineering challenges such as applying a highly homogeneous external magnetic field in alignment with NV⁻ axes²⁵ and improving the cavity Q factor. This has led to efforts to better understand the material and device parameter space which diamond masers inhabit, typically through modeling of spin dynamics with semiclassical rate equations. Here, we use rate equation simulations to investigate how maser performance depends on the properties of the diamond gain medium and the dielectric resonator.

We extend the model beyond the standard first-order rate equations sometimes used to model the photophysics of NV⁻ centers^{15,26} to a system of coupled equations that incorporate the number of photons in the cavity through second-order terms. The extended second-order rate equations incorporate the number of photons in the cavity and allow the time-evolution of the populations of NV⁻ centers in different energy states and the photon number to be simulated explicitly. The rate equations are employed to model the spin-dependent electronic population dynamics of the NV⁻ centers under optical pumping at a wavelength of 532 nm. The results show masing dynamics with various parameters such as the Q factor of the cavity and the mode volume of the resonator. Throughout the paper, “ Q factor” will be taken to refer to the loaded Q factor of the combined resonator-cavity system. As well as aiding the design of

room-temperature diamond masers, the extended rate equations presented will be useful for describing microwave mode-cooling devices²⁷ and quantum heat engines based on NV⁻ centers in diamond.²⁴

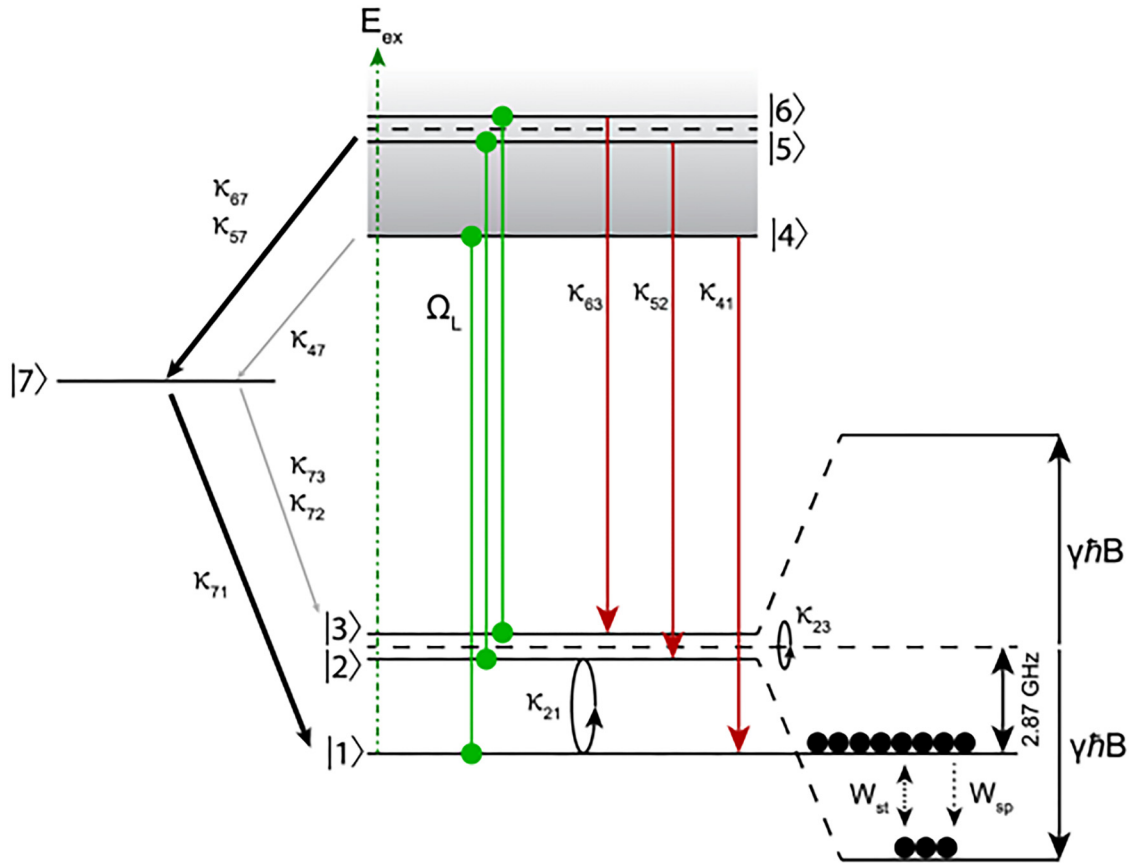
II. THEORETICAL MODEL

The population dynamics of the electronic energy levels of the NV⁻ are described using the seven-level model in Fig. 1, where levels $|1\rangle$ and $|4\rangle$ correspond to the $m_s = 0$ states, and levels $|2\rangle$, $|5\rangle$ and $|3\rangle$, $|6\rangle$ correspond to the $m_s = -1$ and $m_s = +1$, respectively. The spin dynamics of different states under an optical excitation on NV⁻ spin defects are described by rate equations based on a seven-level model and an extended Bloch equation formalism.^{26,28} We model the excitation of NVs with a laser to create a population inversion in diamond masers as an optical pump from the ground-state sublevels $|1\rangle$, $|2\rangle$, and $|3\rangle$, respectively, to the excited-state sublevels $|4\rangle$, $|5\rangle$, and $|6\rangle$ the rate at which NVs are excited by the laser is parameterized by the optical pump rate, defined as

$$\Omega_L = \mathcal{E}\mathbf{D}_{ij}/\hbar, \quad (2)$$

where \mathcal{E} is the electric field of the laser and \mathbf{D}_{ij} is the dipole moment of the induced transition between level $|i\rangle$ and level $|j\rangle$, such as the ground triplet states and the excited triplets. In general, the transition dipole moment for the NV⁻ centers is sensitive to local strain in the diamond lattice and is, therefore, sample dependent. In this paper, we use a dipole moment of 1.73×10^{-29} C m, estimated from a fluorescence lifetime of 13 ns.²⁹ A shorter fluorescence lifetime will have a higher dipole moment. The electric field amplitude is determined by the laser pump power available at the NV⁻ centers with respect to the absorption dipole direction, laser polarization and laser spot size. In diamond masers demonstrated to date, a laser of wavelength 532 nm is used to excite the NV⁻ spin defects from the ground state sub-levels ($|1\rangle$, $|2\rangle$, and $|3\rangle$) to an excited phonon band shown as a gray band in Fig. 1. They subsequently relax nonradiatively to the excited sub-levels $|4\rangle$, $|5\rangle$, and $|6\rangle$. Since the phonon relaxation is generally fast compared to the optical pump rate, the off-resonant pumping is modeled using a common pump rate determined by the optical pump strength Ω_L for these transitions. From the excited states, the NV⁻ centers can either decay radiatively through spin-conserving fluorescence at a wavelength of 637 nm (indicated by red lines with respective decay rates) or non-radiatively via spin-selective intersystem crossing, passing through the spin singlet $|7\rangle$. The decays from excited states to lower energy states $|i\rangle \rightarrow |j\rangle$ have corresponding rates κ_{ij} .

Since $\kappa_{57}, \kappa_{67} \gg \kappa_{47}$, NVs in the $|5\rangle$ and $|6\rangle$ states are much more likely to decay to the intermediate singlet state $|7\rangle$ than those excited to the $|4\rangle$ state and the net result of optically pumping the system is to preferentially fill level $|1\rangle$. In a magnetic field applied along an NV axis whose magnitude exceeds the ground-state level anticrossing point at 102.5 mT, the $m_s = -1$ sub-level ($|2\rangle$) is shifted below $|1\rangle$ so that filling $|1\rangle$ entails a population inversion, as required for masing. For such a population inversion to be maintained the optical pumping must fill the $|1\rangle$ state faster than the longitudinal relaxation rate, κ_{21} , with which the NV ensemble tends towards thermal equilibrium (for which at room temperature the populations of levels $|1\rangle$, $|2\rangle$, and $|3\rangle$ are roughly equal).



22 February 2024 14:16:02

FIG. 1. This NV⁻ energy level diagram indicating pumping and decay rates of the seven-level model with excited phonon bands shown by the gray area in levels —4), —5), and —6). Here, the green dashed line represents the energy of the excitation wavelength (532 nm, 2.33 eV), promoting population to the phonon bands, whereas the green solid line is the transition represented by the pump strength Ω_L . Decay rates are indicated by κ_{ij} (the values for these rates used to generate our results are provided in Table I) for the decay from the initial electronic state i to the new state j , $\gamma\hbar B$ is the Zeeman splitting, and W_{st} and W_{sp} are the stimulated emission rate and the spontaneous emission rate. Non-radiative decays are also shown to, and from, $|7\rangle$ where the bold line denotes the faster decay rate.

The rate equations used to generate our results (shown in the Appendix) can be derived by taking the matrix elements of the Hamiltonian and the density matrix and using them to form von Neumann’s equations of motion, which give the unitary evolution of the seven-level system. The decay rates between the levels are phenomenologically added in diagonal terms,²⁸ representing the populations, whereas the dephasing terms are added in the non-diagonal terms, representing the coherences. The photon number is treated as a second-order rate equation that depends on the number of thermal photons, and the spontaneous and stimulated transition rates. The operating frequency of the maser is the same as the resonant frequency of the cavity. The rate equations thus form equations of motion for density matrix elements expressed with respect to a seven-level Hamiltonian of the form

$$\mathcal{H} = \sum_{i=1}^7 E_i |i\rangle\langle i| + \hbar\Omega_L \sum_{i=1,2,3} (|i\rangle\langle i+3| + |i+3\rangle\langle i|), \quad (3)$$

where E_i is the energy of the i th level, h is the Planck constant, $|i\rangle$ denotes the i th state of the NV⁻ centers (as in Fig. 1). Photons are treated phenomenologically by the addition of a photon term included in the rate equations (see the Appendix for further details). Using rates reported in Ref. 24, the equations of motion were solved numerically using an implicit Runge–Kutta method with a backward differentiation method^{30,31} to simulate the time evolution of a diamond maser.

III. MASER SIMULATION

The seven-level rate equations can be used to predict masing operation when a magnetic field shifts the $m_s = -1$ state ($|2\rangle$) below the $m_s = 0$ state ($|1\rangle$). When optical pumping is employed to create a population inversion between states ($|1\rangle$) and ($|2\rangle$), the NVs will transition between these states to restore thermal equilibrium via spin–lattice relaxation (at a rate κ_{12}) and via the absorption and spontaneous and stimulated emission of microwave (MW)

TABLE I. Transition rates used to describe the time evolution of the ensemble of NV^- centers in a cavity to produce the results presented in Figs. 3–7. The values are based on experimental results from Ref. 24.

Parameters	Values (MHz)
$\kappa_{41} = \kappa_{52} = \kappa_{63}$	65.9
$\kappa_{57} = \kappa_{67}$	53.3
κ_{47}	7.9
κ_{71}	0.98
$\kappa_{72} = \kappa_{73}$	0.73
$\kappa_{21} = \kappa_{23}$	4.4×10^{-4}

photons. For microwave-frequency transitions, the spin–lattice relaxation rate, on the order of 10^2 Hz, is much higher than the spontaneous emission rate in free space, which is on the order of 10^{-13} Hz.³² Hence the spins preferentially relax by transferring energy to the lattice. The spontaneous emission rate is described using Einstein coefficients **A** and **B**, which phenomenologically describes the rate of the spontaneous and stimulated emission processes and can be boosted through the Purcell effect depending on the cavity Q factor.

The transition rate from one state i to another state j is determined³³ by the magnetic dipole matrix element of the corresponding two states, $\mathbf{D}_{ij} = \langle j | \mathbf{H} \cdot \mathbf{S} | i \rangle$, where \mathbf{H} is the MW magnetic field and \mathbf{S} is the spin vector, and the density of states of the electromagnetic field, $\rho(\omega)$ as $W \propto \frac{|\mathbf{D}_{ij}|^2 \rho(\omega)}{\hbar}$. The magnetic field is approximated as a classical perturbation so that the matrix element is replaced by σ_{ij} , which denotes a matrix element for the spin transition, so its square-modulus is proportional to a transition probability, and the dipole matrix element is $(\mathbf{H} \langle j | \mathbf{S} | i \rangle)^2 = (\mathbf{H} \sigma_{ij})^2$. When the NV ensemble is placed in a cavity, the density of microwave photon states at the masing frequency is altered with respect to its free-space value, causing a proportionate shift in the spontaneous and stimulated emission rates for the maser transition. This change in these rates is equal to the Purcell factor, $F = \frac{3c^3}{2\pi\omega^3 n_{re}^3} \frac{Q}{V_m}$, where c is

TABLE II. Variable parameters used in the rate equations to describe the time evolution of the ensemble of NV^- centers in a cavity. The number of available NV^- , the maser frequency, ω , the dephasing time, T_2^* , and the Q factor is from Ref. 10. V_m and η are obtained in a CST MICROWAVE STUDIO simulation. Δ_l is the detuning in frequency between the 532 nm excitation laser and the zero phonon line at 637 nm and Ω_L is the estimated pump strength at 400 mW of excitation power.

Parameters	Values
N	4×10^{13}
ω	$2\pi \times 9.22$ GHz
T_2^*	0.5 μ s
V_m	0.25 cm ³
Q	30,000
η	0.05
B	432 mT
Δ_l	92.89 THz
Ω_L	1150.7 MHz

the speed of light, ω is the cavity resonance frequency, V_m is the mode volume, and n_{re} is the refractive index in the cavity.³² To enhance the spontaneous emission rate for a given frequency, a high Q factor and a small mode volume are thus required.

In the masing simulation, the initial photon number in the cavity is determined by the thermal photon number at thermal equilibrium, $n_{th} = (e^{\hbar\omega/k_B T} - 1)^{-1}$. There is no external microwave input. At 9.22 GHz and room temperature, $n_{th} \approx 635$, and these initial MW photons are able to be absorbed or trigger stimulated emission.

The stimulated emission rate per intracavity photon is given at resonance by^{27,34}

$$W_{st} = \frac{\pi(g\mu_B)^2 \mu_0 T_2^* \omega \eta}{4\pi\hbar V_m}, \quad (4)$$

where the filling factor η and the mode volume V_m are, respectively, defined by

$$\eta = \frac{\int_{Sample} |\mathbf{H}|^2 dV}{\int_{Mode} |\mathbf{H}|^2 dV}, \quad (5)$$

$$V_m = \frac{\int_{Cavity} |\mathbf{H}|^2 dV}{|\mathbf{H}_{Max}|^2}. \quad (6)$$

The higher the filling factor, the more strongly the sample interacts with the cavity mode. The numerator of the mode volume is integrated over the entire copper cavity volume, including the dielectric resonator.

For the results presented in the following section, the parameters from Tables I and II are used. The finite-element software CST MICROWAVE STUDIO is used to estimate the mode volume and the filling factor, using Eqs. (5) and (6). In the CST MICROWAVE STUDIO simulation, we model a system similar to that used to demonstrate masing from an NV-enriched diamond sample with a resonant frequency of 9.22 GHz, employing a sapphire resonator with an inner diameter of 5 mm, an outer diameter of 10 mm and a height of 6 mm on a sapphire post of 12 mm high and enclosed in a copper cavity with an inner diameter of 31 mm and a height of 30 mm. The dielectric constant of the sapphire was set to 9.4, the loss tangent to 8×10^{-6} .³⁵ The dielectric constant ϵ determines the size of the resonator and the mode volume with $V_m \propto 1/\epsilon^{3/2}$, while the loss tangent affects the Q factor. Dielectric materials with a high dielectric constant and a small loss tangent are favorable, as this increases the Purcell factor. The energy density of the magnetic field of the TE_{01 δ} mode of the cavity is shown in Fig. 2. W_{st} is approximately $1.98 \times 10^{-6} \text{ s}^{-1}$. The spontaneous rate is given by³⁴

$$W_{sp} = \frac{\mu_0 \omega^3 (g\mu_B)^2}{6\pi\hbar c^3}. \quad (7)$$

At 9.22 GHz, the spontaneous emission rate is about $1.57 \times 10^{-12} \text{ s}^{-1}$, which is much slower than the stimulated transition rate and the spin relaxation rate.

The optical pumping strength, Ω_L , is 1150.7 MHz, which corresponds to 400 mW of optical power. The initial populations of the NV energy levels are set by the Boltzmann distribution, with each state filled with a population proportional to $e^{-E_i/k_B T}$, where k_B is the Boltzmann constant, T is the temperature, and E_i the energy of the $|i\rangle$ state. The initial number of MW photons is $(e^{h\omega/k_B T} - 1)^{-1}$ with ω being the frequency of the cavity field and maser output, equal to the frequency of the transition between $|1\rangle$ and $|2\rangle$.

Looking at the intracavity photon number as a function of the cavity Q factor (Fig. 3), with other parameters fixed, we identify a masing threshold as the point where the number of photons in the cavity is an order of magnitude greater than the thermal population. The maser output power, in Watts, can be estimated using $n\hbar\omega^2/Q_m$, where ω is the operating maser frequency, n is the intracavity photon number (of order 10^5 when the maser is just above the threshold), and $Q_m = 1/(1/Q_l - 1/Q_u)$, where Q_l and Q_u are the loaded and unloaded Q factors, is the contribution of the diamond to the loaded Q factor. For realistic values of $Q_l = 30\,000$ and $Q_u = 50\,000$ the maser output is thus around 0.5 pW, or -93 dBm. By incorporating the loaded and unloaded Q factors, the output coupling efficiency of the system is already taken into account so this can be directly compared to data from Ref. 10, which measured an output power of -90 dBm. With a lower Q factor, the number of photons will be closer to the thermal photon number, suppressing any maser action. As the Q factor increases, the number of cavity photons also increases until at a certain threshold Q factor, the number of photons increases significantly. Beyond this point, the photon emission rate is higher than the cavity decay rate, thus, the number of photons in the cavity is

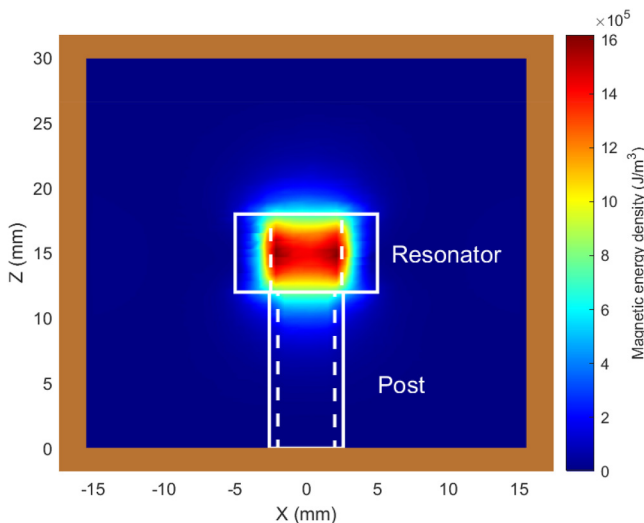


FIG. 2. The energy density of the magnetic field of the $TE_{01\delta}$ mode of a cylindrical copper cavity simulated using CST MICROWAVE STUDIO. The solid white outlines show the boundaries of a sapphire resonator and post, and the dashed white outlines the inner boundaries. The walls of the copper cavity are shown as the enclosure that bounds the image.

stable at a level significantly higher than the thermal photon background and will not decay away since in this case emission is predominantly stimulated and balanced by absorption at the same rate. In Fig. 4, the performance of the maser at different optical pump powers is studied at a fixed Q factor of 30 000. For the parameters employed, the maser starts to operate above a threshold pump power of 370 mW. Despite using different diamond material parameters, the threshold Q factor and the threshold pump power are similar to those from recent experimental results reported in Ref. 17.

The threshold behavior with respect to the mode volume, which is inversely proportional to the Purcell factor and the cooperativity, is shown in Fig. 5. As expected, smaller mode volumes increase the number of masing photons in the cavity. For the parameters in Tables I and II, the threshold is roughly at 0.27 cm^3 , and for larger mode volumes masing cannot occur.

Figure 6 shows the contour map of the number of photons as a function of the optical pump power and the Q factor. The dark blue region shows that the masing effect does not occur due to the high losses and low pump power. The second region, in dark green, shows the “incipient masing” region, where stimulated emission starts to build up and the number of photons is higher than the number of thermal photons. In this region, an external MW signal fed into the maser would be amplified but the maser cannot be run as an oscillator. The maser is in operation in the light green region, where stimulated emission is maintained and the device can undergo self-sustaining maser oscillations.

The number of intracavity photons is shown as a function of the gain medium filling factor, defined in Eq. (5), in Fig. 7, again displaying a clear threshold for masing. The results show that the

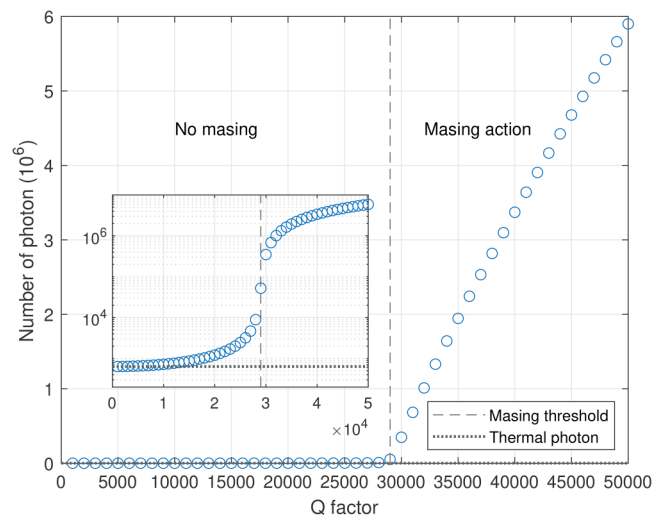


FIG. 3. The steady-state number of photons as a function of the cavity Q factor. The photon number shows threshold behavior with respect to the Q factor, with the onset of masing at around $Q = 29\,000$ for the parameters listed in Table I. The inset shows the onset on a logarithmic scale.

22 February 2024 14:16:02

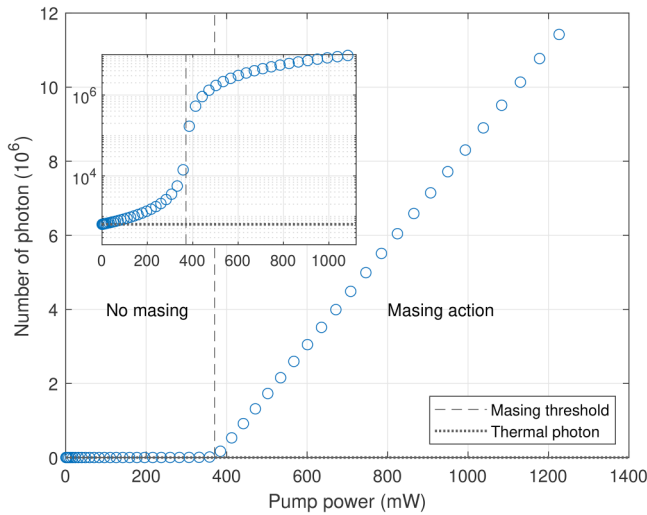


FIG. 4. The steady-state number of photons as a function of the optical pump power. For the parameters listed in Table I, the threshold pump power is about 370 mW.

threshold is about 0.03, beyond which the number of photons maintained in the cavity significantly increases beyond the thermal population. The number of cavity photons increases monotonically as the filling factor approaches unity.

It is assumed that the number of NV⁻ centers is constant during masing. This is reasonable for pump powers around the masing thresholds observed since these are low enough that the

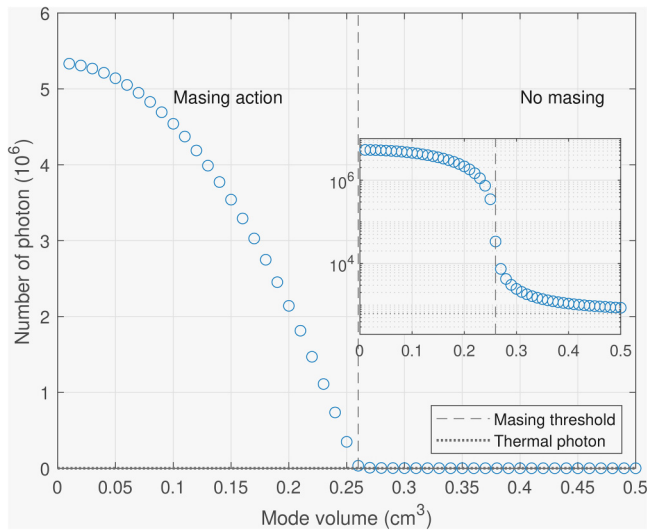


FIG. 5. The steady-state number of microwave photons as a function of the cavity mode volume for the parameters listed in Table I. The masing threshold occurs at a mode volume of about 0.26 cm³. The inset shows the onset on a logarithmic scale.

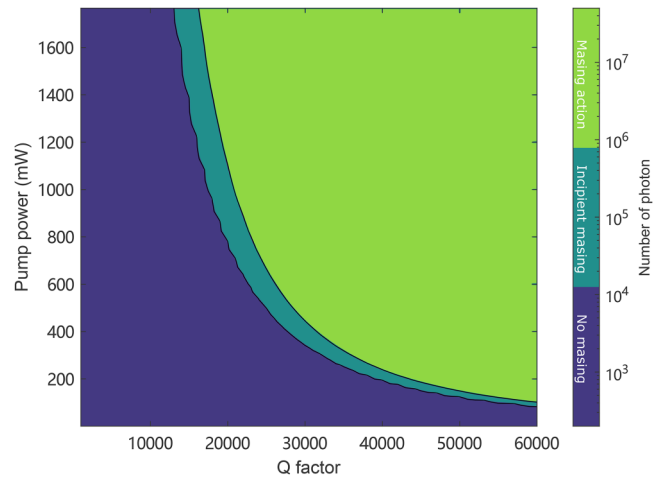


FIG. 6. The steady-state microwave photon number as a function of the optical pump strength and the loaded cavity Q factor. We identify a masing action regime, a no masing regime, and an intermediate “incipient masing” regime in which stimulated emission dominates spontaneous emission, but the maser cannot achieve self-sustaining oscillations. At all pump strengths, the photon number increases monotonically with the Q factor as expected.

ionization and recombination of NV centers due to laser excitation is expected to be weak.^{23,36} Similarly, all the rates are assumed to be constant, neglecting any heating which will lead to a reduction in T_1 time¹⁷ as well as the T_2 time.³⁷ Both of these spin lifetimes vary with temperature as T^5 , though the T_2^* lifetime caused by the field inhomogeneity is only very weakly dependent on temperature.³⁷

22 February 2024 14:16:02

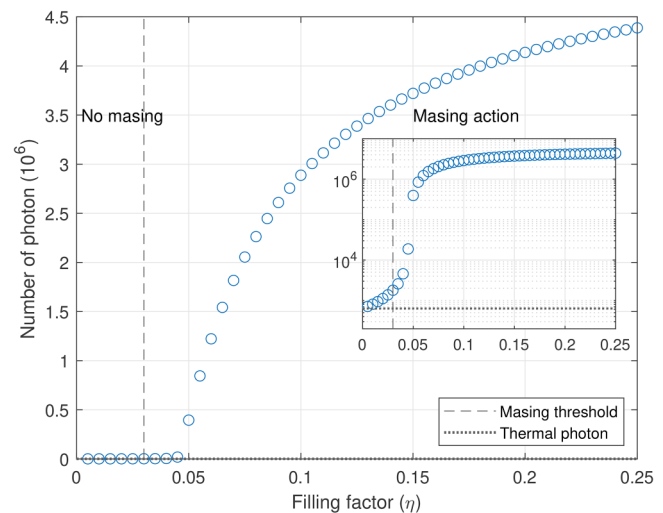


FIG. 7. The number of microwave photons in the cavity as a function of the filling factor, defined by Eq. (4). The number of photons becomes saturated above $\eta = 0.3$. The inset shows the onset of masing at a filling factor of 0.03.

The zero-field splitting is also temperature dependent,³⁸ but since this effect is weak (cooling from room temperature to 4 K, causes a change of less than 1% in the zero-field splitting), it is ignored in this model. All these temperature effects will tend to broaden the maser linewidth. Recent work has shown that the high power rate will significantly increase the temperature, especially the T_1 time, which makes maser action impossible¹⁷ by affecting the ability of the gain medium to maintain a population inversion. It would be interesting to develop the rate equation approach presented here to include such effects, though they are expected to lead only to small changes in the predicted thresholds.

A further interesting extension to our rate equation model would be to explicitly model the effect of NV concentration on the spin lifetimes. To first order, changes in the NV^- concentration does not affect the cooperativity since the spin decay rate κ_s is proportional to the NV^- concentration³⁹ so that the factor of N/κ_s in the cooperativity is constant. However, the concentration of NV^- in diamond samples depends not just on the concentration of nitrogen impurities but on the efficiency with which such impurities can be converted to nitrogen-vacancy centers. The relative populations of the two possible charge states (NV^- and NV^0), each of which can have an independent effect on the spin decay rate, implies the cooperativity is not independent of the $[NV^-]$ for real systems. The ratio of $NV^0:NV^-$ is typically¹⁰ around 14:1, but a ratio of 6.95:1 has been reported for an optimized system.⁴⁰ It is also important to note that the diamond sample can have spatially varying concentrations. Finally, we expect a higher concentration to lead to increased self-absorption,⁴¹ which is not taken into account in our model but will again tend to increase the threshold pump power by increasing the effective cavity decay rate.

Since the uniformity of applied magnetic fields is a key barrier to the miniaturization of diamond masers, an important question is how field inhomogeneity affects the masing thresholds. The homogeneous linewidth of the NV^- resonance is about 1 MHz⁴² and in these simulations, it is assumed that the spatial inhomogeneity of the applied magnetic field over the volume of the diamond is small enough that the resulting Zeeman shifts are within the homogeneous linewidths of the NV^- centers. For an intrinsic linewidth of 1 MHz, this means the field inhomogeneity should be <0.03 mT. For experimental systems, smaller field inhomogeneity increases the number of NV spins in resonance with the cavity, increasing the cooperativity and reducing the pumping threshold.

IV. CONCLUSION

We have used rate equations extended to second-order to incorporate the intracavity photon number and coherences between different NV energy states to simulate the spin dynamics of an ensemble of NV^- centers in a diamond-based maser. The model predicts the behavior of the maser as a function of material parameters of the gain medium and resonator in good agreement with recent experimental results.¹⁷

Cooperativity (and the related Purcell factor) are identified as key quantities which, if increased, will reduce the threshold pump power for masing. On the one hand, this requires a high Q factor and a small mode volume, but intrinsic material parameters of the diamond gain media such as the concentration of NV^- and T_2^*

play a significant role, where a long T_2^* and more excited spins, which are determined by the filling factor and the concentration of the sample, are favorable. Ever higher pump powers will eventually reduce the number of maser photons, as the populations end up in the singlet state and the population inversion is reduced due to a kinetic bottleneck leading to the accumulation of NV^- centers in the $|7\rangle$ state, so optimizing the cooperativity to lower the threshold pump power will be important for developing scalable diamond masers. Alternatively, increasing the transition rate from the $|7\rangle$ state through Purcell enhancement of a 1042 nm transition between two sub-levels of $|7\rangle$ could thus be a pathway to higher maser power outputs, though this is beyond the scope of our model. Attention to these considerations will aid the design of diamond-based masers suitable for mass production.

Additionally, we have suggested further improvements in the modeling of NV^- ensembles for maser applications. If the NV^- to NV^0 charge conversion and the effects of temperature and NV^- concentration on the spin lifetimes are considered, the trade-offs between maximizing the coherence times and increasing output power and cooperativity by maximizing the number of NV^- centers and the pump power will become clearer. Such improvements will require further experimental input, particularly on the relationship between charge-state ratios and spin lifetimes.

The method presented in this paper, which computes the time evolution of the maser output explicitly, will be of particular use for describing the “incipient masing” regime where the stimulated emission is dominant over the spontaneous emission, but insufficient for self-sustaining maser oscillation and thus less amenable to solutions based on steady-state considerations. The full time-dependent response of diamond masers will also be useful for technological applications where masers are used to amplify arbitrary time-dependent microwave signals.

More broadly, we anticipate that the model presented in this paper will be of use for improved modeling of other quantum technologies based on ensembles of spin defects, such as diamond magnetometers³ and room-temperature masers based on alternative gain media such as silicon-vacancy defects in SiC.^{43–45}

SUPPLEMENTARY MATERIAL

Example Matlab code to compute the time evolution of a diamond maser using the equations for $\partial\rho/\partial t$ presented in the Appendix is included as Supplementary Material in the form a simple function `drhodt`, which outputs the components of ρ and the photon number, respectively, over a specified time interval.

ACKNOWLEDGMENTS

This work was supported by the UK Engineering and Physical Sciences Research Council through the NAME Programme Grant (No. EP/V001914/1) and through Grant No. EP/S000798/1. The authors further wish to acknowledge support from the Henry Royce Institute and helpful discussions with Dr. Wern Ng.

AUTHOR DECLARATIONS

Conflict of Interest

The authors have no conflicts to disclose.

Author Contributions

Yongqiang Wen: Conceptualization (equal); Investigation (equal); Software (equal); Validation (equal); Visualization (lead); Writing – original draft (lead); Writing – review & editing (equal). **Philip L. Diggle:** Validation (equal); Visualization (equal); Writing – review & editing (equal). **Neil McN. Alford:** Supervision (equal); Visualization (equal); Writing – review & editing (equal). **Daan M. Arroo:** Conceptualization (lead); Investigation (equal); Methodology (equal); Supervision (equal); Validation (equal); Writing – original draft (equal); Writing – review & editing (equal).

$$\rho = \begin{pmatrix} \rho_{11} \\ \rho_{22} \\ \rho_{33} \\ \rho_{44} \\ \rho_{55} \\ \rho_{66} \\ \rho_{77} \\ \rho_{14} \\ \rho_{41} \\ \rho_{25} \\ \rho_{52} \\ \rho_{63} \\ \rho_{36} \end{pmatrix},$$

DATA AVAILABILITY

The data that support the findings of this study are available from the corresponding author upon reasonable request.

APPENDIX: MATRIX EQUATIONS

Using the Hamiltonian, Eq. (3), and the von Neumann equations of motion,

$$i\hbar \frac{d\rho}{dt} = [\mathcal{H}, \rho], \tag{A1}$$

where ρ is a 7×7 density matrix. Substituting into the von Neumann equations, the time-derivative of the density matrix has 13 non-zero elements.

We present the rate equations solved numerically to generate the results of this work in the matrix form. The overall equation of motion for the vectorized density matrix, which only contains 13 terms, ρ is given by

$$\dot{\rho} = M\rho$$

$$M = \begin{bmatrix} M_{11} & M_{12} \\ M_{21} & M_{22} \end{bmatrix},$$

where M_{ij} are sub-matrices of M used to clarify the equation by separating different contributions to the time evolution. M_{11} is the 7×7 population sub-matrix, describing the spin dynamics of the seven-level model. M_{12} and M_{21} are the population-coupling sub-matrices, respectively, 6×7 and 7×6 , that describe the coupling of the laser field and the MW field with the seven-level model. Finally, M_{22} is the coherence sub-matrix that describes the coherence of the coupled fields. This 13×13 matrix contains seven non-zero diagonal terms and six non-diagonal terms. ρ_{ij} represents the element of the density matrix, the diagonal terms represent the populations, and the off-diagonal terms represent the coherence terms. The sub-matrices are given explicitly as

$$M_{22} = \begin{bmatrix} -\gamma_l + i\Delta_l & 0 & 0 & 0 & 0 & 0 & 0 \\ 0 & -\gamma_l + i\Delta_l & 0 & 0 & 0 & 0 & 0 \\ 0 & 0 & -\gamma_l + i\Delta_l & 0 & 0 & 0 & 0 \\ 0 & 0 & 0 & -\gamma_l + i\Delta_l & 0 & 0 & 0 \\ 0 & 0 & 0 & 0 & -\gamma_l + i\Delta_l & 0 & 0 \\ 0 & 0 & 0 & 0 & 0 & -\gamma_l + i\Delta_l & 0 \\ 0 & 0 & 0 & 0 & 0 & 0 & -\gamma_l + i\Delta_l \end{bmatrix},$$

$$M_{11} = \begin{bmatrix} -2\kappa_{21} & \kappa_{21} & \kappa_{21} & \kappa_{41} & 0 & 0 & \kappa_{71} \\ \kappa_{21} & -2\kappa_{21} & \kappa_{21} & 0 & \kappa_{52} & 0 & 0 \\ \kappa_{21} & \kappa_{21} & -2\kappa_{21} & 0 & 0 & \kappa_{63} & \kappa_{73} \\ 0 & 0 & 0 & -(\kappa_{41} + \kappa_{47}) & 0 & 0 & 0 \\ 0 & 0 & 0 & 0 & -(\kappa_{52} + \kappa_{57}) & 0 & 0 \\ 0 & 0 & 0 & 0 & 0 & -(\kappa_{63} + \kappa_{67}) & 0 \\ 0 & 0 & 0 & \kappa_{47} & \kappa_{57} & \kappa_{67} & -(\kappa_{71} + \kappa_{72} + \kappa_{73}) \end{bmatrix},$$

22 February 2024 14:16:02

$$\mathbf{M}_{12} = \begin{bmatrix} -\frac{\Omega_L}{2}i & \frac{\Omega_L}{2}i & 0 & 0 & 0 & 0 \\ 0 & 0 & -\frac{\Omega_L}{2}i & \frac{\Omega_L}{2}i & 0 & 0 \\ 0 & 0 & 0 & 0 & -\frac{\Omega_L}{2}i & \frac{\Omega_L}{2}i \\ \frac{\Omega_L}{2}i & -\frac{\Omega_L}{2}i & 0 & 0 & 0 & 0 \\ 0 & 0 & \frac{\Omega_L}{2}i & -\frac{\Omega_L}{2}i & 0 & 0 \\ 0 & 0 & 0 & 0 & \frac{\Omega_L}{2}i & -\frac{\Omega_L}{2}i \\ 0 & 0 & 0 & 0 & 0 & 0 \end{bmatrix},$$

$$\mathbf{M}_{21} = \begin{bmatrix} -\frac{\Omega_L}{2}i & 0 & 0 & 0 & \frac{\Omega_L}{2}i & 0 & 0 \\ \frac{\Omega_L}{2}i & 0 & 0 & 0 & -\frac{\Omega_L}{2}i & 0 & 0 \\ 0 & -\frac{\Omega_L}{2}i & 0 & 0 & 0 & \frac{\Omega_L}{2}i & 0 \\ 0 & \frac{\Omega_L}{2}i & 0 & 0 & 0 & -\frac{\Omega_L}{2}i & 0 \\ 0 & 0 & -\frac{\Omega_L}{2}i & 0 & 0 & 0 & \frac{\Omega_L}{2}i \\ 0 & 0 & \frac{\Omega_L}{2}i & 0 & 0 & 0 & -\frac{\Omega_L}{2}i \end{bmatrix},$$

where γ_l is the decoherence rate of the laser-coupled states, and Δ_l is the detuning of the laser from the transition frequencies for $1 \rightarrow 4$, $2 \rightarrow 5$, and $3 \rightarrow 6$.

In the extended rate equations, the NV^- center is treated quantum mechanically as a seven-level system and an additional second-order term, representing the number of photons a , is added to the first-order rate equations,

$$\frac{da}{dt} = F(W_{sp}\rho_{11} + W_{st}(\rho_{11} - \rho_{22})a) - \kappa_c(a - n_{th}),$$

$$\frac{d\rho_{11}}{dt} = (M\rho)_{11} + F(-W_{sp}\rho_{11} - W_{st}a\rho_{11} + W_{st}a\rho_{22}),$$

$$\frac{d\rho_{22}}{dt} = (M\rho)_{22} + F(W_{sp}\rho_{11} + W_{st}a\rho_{11} - W_{st}a\rho_{22}),$$

where W_{sp} is the spontaneous emission rate and W_{st} is the stimulated emission rate. The initial conditions are $\rho_{11} = \rho_{22} = \rho_{33} = N/3$, $a = n_{th}$, where N is the total number of available NV centers, and n_{th} is the number of thermal photons. All other elements of ρ are initially set to zero.

REFERENCES

- ¹A. M. Zaitsev, *Optical Properties of Diamond* (Springer-Verlag, Berlin, 2001).
- ²M. W. Doherty, N. B. Manson, P. Delaney, F. Jelezko, J. Wrachtrup, and L. C. Hollenberg, "The nitrogen-vacancy colour centre in diamond," *Phys. Rep.* **528**, 1–45 (2013).
- ³J. F. Barry, J. M. Schloss, E. Bauch, M. J. Turner, C. A. Hart, L. M. Pham, and R. L. Walsworth, "Sensitivity optimization for NV-diamond magnetometry," *Rev. Mod. Phys.* **92**, 015004 (2020).
- ⁴S. M. Graham, A. T. M. A. Rahman, L. Munn, R. L. Patel, A. J. Newman, C. J. Stephen, G. Colston, A. Nikitin, A. M. Edmonds, D. J. Twitchen, M. L. Markham, and G. W. Morley, "Fiber-coupled diamond magnetometry with an unshielded 30 pT/ $\sqrt{\text{Hz}}$ sensitivity," [arXiv:2211.09170](https://arxiv.org/abs/2211.09170) [physics.app-ph] (2023).
- ⁵R. Patel, L. Zhou, A. Frangeskou, G. Stimpson, B. Breeze, A. Nikitin, M. Dale, E. Nichols, W. Thornley, B. Green *et al.*, "Subnanotesla magnetometry with a fiber-coupled diamond sensor," *Phys. Rev. Appl.* **14**, 044058 (2020).
- ⁶M. Ruf, N. H. Wan, H. Choi, D. Englund, and R. Hanson, "Quantum networks based on color centers in diamond," *J. Appl. Phys.* **130**, 070901 (2021).
- ⁷B. Hensen, H. Bernien, A. E. Dréau, A. Reiserer, N. Kalb, M. S. Blok, J. Ruitenberg, R. F. Vermeulen, R. N. Schouten, C. Abellán *et al.*, "Loophole-free Bell inequality violation using electron spins separated by 1.3 kilometres," *Nature* **526**, 682–686 (2015).
- ⁸C. E. Bradley, J. Randall, M. H. Abobeih, R. Berrevoets, M. J. Degen, M. A. Bakker, M. Markham, D. J. Twitchen, and T. H. Taminiau, "A ten-qubit solid-state spin register with quantum memory up to one minute," *Phys. Rev. X* **9**, 031045 (2019).
- ⁹J. Weber, W. Koehl, J. Varley, A. Janotti, B. Buckley, C. Van de Walle, and D. D. Awschalom, "Quantum computing with defects," *Proc. Natl. Acad. Sci. U.S.A.* **107**, 8513–8518 (2010).
- ¹⁰J. D. Breeze, E. Salvadori, J. Sathian, N. M. Alford, and C. W. Kay, "Continuous-wave room-temperature diamond maser," *Nature* **555**, 493–496 (2018).
- ¹¹M. Oxborrow, J. D. Breeze, and N. M. Alford, "Room-temperature solid-state maser," *Nature* **488**, 353–356 (2012).
- ¹²W. Ng, X. Xu, M. Attwood, H. Wu, Z. Meng, X. Chen, and M. Oxborrow, "Move aside pentacene: Diazapentacene doped para-terphenyl, a zero-field room-temperature maser with strong coupling for cavity quantum electrodynamics," *Adv. Mater.* **35**, 2300441 (2023).
- ¹³M. Attwood, X. Xu, M. Newns, Z. Meng, R. Ingle, H. Wu, X. Chen, W. Xu, W. Ng, T. Abiola, V. Stavros, and M. Oxborrow, "N-heteroacenes as an organic gain medium for room temperature masers," *ChemRxiv* (2023).
- ¹⁴L. Jin, M. Pfender, N. Aslam, P. Neumann, S. Yang, J. Wrachtrup, and R.-B. Liu, "Proposal for a room-temperature diamond maser," *Nat. Commun.* **6**, 1–8 (2015).
- ¹⁵A. Sherman, L. Buchbinder, S. Ding, and A. Blank, "Performance analysis of diamond-based masers," *J. Appl. Phys.* **129**, 144503 (2021).
- ¹⁶A. Sherman, O. Zgzdzai, B. Koren, I. Peretz, E. Laster, and A. Blank, "Diamond-based microwave quantum amplifier," *Sci. Adv.* **8**, eade6527 (2022).
- ¹⁷C. W. Zollitsch, S. Ruloff, Y. Fett, H. T. Wiedemann, R. Richter, J. D. Breeze, and C. W. Kay, "Maser threshold characterization by resonator Q-factor tuning," *arXiv preprint arXiv:2302.10811* (2023).
- ¹⁸D. M. Arroyo, N. M. Alford, and J. D. Breeze, "Perspective on room-temperature solid-state masers," *Appl. Phys. Lett.* **119**, 140502 (2021).

- ¹⁹A. Roy and M. Devoret, "Introduction to parametric amplification of quantum signals with Josephson circuits," *C. R. Phys.* **17**, 740–755 (2016).
- ²⁰A. Jarmola, V. Acosta, K. Jensen, S. Chemerisov, and D. Budker, "Temperature- and magnetic-field-dependent longitudinal spin relaxation in nitrogen-vacancy ensembles in diamond," *Phys. Rev. Lett.* **108**, 197601 (2012).
- ²¹G. Balasubramanian, P. Neumann, D. Twitchen, M. Markham, R. Kolesov, N. Mizuochi, J. Isoya, J. Achard, J. Beck, J. Tissler *et al.*, "Ultralong spin coherence time in isotopically engineered diamond," *Nat. Mater.* **8**, 383–387 (2009).
- ²²P. L. Stanwix, L. M. Pham, J. R. Maze, D. Le Sage, T. K. Yeung, P. Cappellaro, P. R. Hemmer, A. Yacoby, M. D. Lukin, and R. L. Walsworth, "Coherence of nitrogen-vacancy electronic spin ensembles in diamond," *Phys. Rev. B* **82**, 201201 (2010).
- ²³A. Savvin, A. Dormidonov, E. Smetanina, V. Mitrokhin, E. Lipatov, D. Genin, S. Potanin, A. Yeliseyev, and V. Vins, "NV⁻ diamond laser," *Nat. Commun.* **12**, 7118 (2021).
- ²⁴J. Klatzow, J. N. Becker, P. M. Ledingham, C. Weinzetl, K. T. Kaczmarek, D. J. Saunders, J. Nunn, I. A. Walmsley, R. Uzdin, and E. Poem, "Experimental demonstration of quantum effects in the operation of microscopic heat engines," *Phys. Rev. Lett.* **122**, 110601 (2019).
- ²⁵A. Patel, Z. Chowdhry, A. Prabhakar, and V. P. Bhallamudi, "Assembling a diamond MASER," in *2021 IEEE Research and Applications of Photonics in Defense Conference (RAPID)* (IEEE, 2021).
- ²⁶K. Jensen, V. Acosta, A. Jarmola, and D. Budker, "Light narrowing of magnetic resonances in ensembles of nitrogen-vacancy centers in diamond," *Phys. Rev. B* **87**, 014115 (2013).
- ²⁷W. Ng, H. Wu, and M. Oxborrow, "Quasi-continuous cooling of a microwave mode on a benchtop using hyperpolarized NV- diamond," *Appl. Phys. Lett.* **119**, 234001 (2021).
- ²⁸I. Popa, "Pulsed magnetic resonance on single defect centers in diamond," Ph.D. thesis (Fakultät Mathematik und Physik der Universität Stuttgart, 2006).
- ²⁹A. Alkauskas, B. B. Buckley, D. D. Awschalom, and C. G. Van de Walle, "First-principles theory of the luminescence lineshape for the triplet transition in diamond NV centres," *New J. Phys.* **16**, 073026 (2014).
- ³⁰W. T. Vetterling, W. H. Press, S. A. Teukolsky, and B. P. Flannery, *Numerical Recipes: The Art of Scientific Computing* (Cambridge University Press, 2002).
- ³¹M. Hosea and L. Shampine, "Analysis and implementation of TR-BDF2," *Appl. Numer. Math.* **20**, 21–37 (1996).
- ³²E. M. Purcell, "Spontaneous emission probabilities at radio frequencies," in *Confined Electrons and Photons* (Springer, 1995), pp. 839–839.
- ³³V. B. Berestetskii, E. M. Lifshitz, and L. P. Pitaevskii, *Quantum Electrodynamics: Volume 4* (Butterworth-Heinemann, 1982), Vol. 4.
- ³⁴A. E. Siegman, *Microwave Solid-State Masers* (McGraw-Hill Book Company, 1964).
- ³⁵J. Breeze, *Temperature and Frequency Dependence of Complex Permittivity in Metal Oxide Dielectrics: Theory, Modelling and Measurement* (Springer, 2016).
- ³⁶I. Cardoso Barbosa, J. Gutsche, and A. Widera, "Impact of charge conversion on NV-center relaxometry," [arXiv:2301.01063](https://arxiv.org/abs/2301.01063) (2023).
- ³⁷S. Lin, C. Weng, Y. Yang, J. Zhao, Y. Guo, J. Zhang, L. Lou, W. Zhu, and G. Wang, "Temperature-dependent coherence properties of NV ensemble in diamond up to 600 K," *Phys. Rev. B* **104**, 155430 (2021).
- ³⁸X.-D. Chen, C.-H. Dong, F.-W. Sun, C.-L. Zou, J.-M. Cui, Z.-F. Han, and G.-C. Guo, "Temperature dependent energy level shifts of nitrogen-vacancy centers in diamond," *Appl. Phys. Lett.* **99**, 161903 (2011).
- ³⁹Z.-H. Wang and S. Takahashi, "Spin decoherence and electron spin bath noise of a nitrogen-vacancy center in diamond," *Phys. Rev. B* **87**, 115122 (2013).
- ⁴⁰A. M. Edmonds, C. A. Hart, M. J. Turner, P.-O. Colard, J. M. Schloss, K. S. Olsson, R. Trubko, M. L. Markham, A. Rathmill, B. Horne-Smith *et al.*, "Characterisation of CVD diamond with high concentrations of nitrogen for magnetic-field sensing applications," *Mater. Quantum Technol.* **1**, 025001 (2021).
- ⁴¹T.-S. Ahn, R. O. Al-Kaysi, A. M. Müller, K. M. Wentz, and C. J. Bardeen, "Self-absorption correction for solid-state photoluminescence quantum yields obtained from integrating sphere measurements," *Rev. Sci. Instrum.* **78**, 086105 (2007).
- ⁴²B. Fortman and S. Takahashi, "Understanding the linewidth of the ESR spectrum detected by a single NV center in diamond," *J. Phys. Chem. A* **123**, 6350–6355 (2019).
- ⁴³H. Kraus, V. Soltamov, D. Riedel, S. Vâth, F. Fuchs, A. Sperlich, P. Baranov, V. Dyakonov, and G. Astakhov, "Room-temperature quantum microwave emitters based on spin defects in silicon carbide," *Nat. Phys.* **10**, 157–162 (2014).
- ⁴⁴M. Fischer, A. Sperlich, H. Kraus, T. Ohshima, G. Astakhov, and V. Dyakonov, "Highly efficient optical pumping of spin defects in silicon carbide for stimulated microwave emission," *Phys. Rev. Appl.* **9**, 054006 (2018).
- ⁴⁵A. Gottscholl, M. Wagenhöfer, M. Klimmer, S. Scherbel, C. Kasper, V. Baianov, G. V. Astakhov, V. Dyakonov, and A. Sperlich, "Superradiance of spin defects in silicon carbide for maser applications," *Front. Photonics* **3**, 886354 (2022).